

Final Draft
of the original manuscript:

Froend, M.; Ventzke, V.; Riekehr, S.; Kashaev, N.; Klusemann, B.; Enz, J.:
**Microstructure and microhardness of wire-based laser metal deposited
AA5087 using an Ytterbium fibre laser.**

In: Materials Characterization. Vol. 143 (2018) 59 - 67.

First published online by Elsevier: May 22, 2018

DOI: /10.1016/j.matchar.2018.05.022

<https://dx.doi.org/10.1016/j.matchar.2018.05.022>

Microstructure and microhardness of wire-based laser metal deposited AA5087 using an Ytterbium fibre laser

M. Froend^{a,b,*}, V. Ventzke^b, S. Riekehr^b, N. Kashaev^b, B. Klusemann^{a,b}, J. Enz^b

^aLeuphana University of Lueneburg, Institute of Product and Process Innovation, Volgershall 1, D-21339 Lueneburg, Germany

^bHelmholtz-Zentrum Geesthacht, Institute of Materials Research, Materials Mechanics, Joining and Assessment Department, Max-Planck-Strasse 1, D-21502 Geesthacht, Germany

Abstract

Wire-based laser metal deposition as a part of additive manufacturing evolved to a state of the art methodology in industry during the last decades. Although it is nowadays possible to manufacture structures, which are free from inner defects such as porosity and cracks, there is still a lack of knowledge regarding the influence of the deposition strategy and process parameters on the mechanical properties of the resulting structure. The following work contains a microstructural and mechanical characterization of an unidirectional manufactured AA5087 aluminium alloy structure on AA5754 substrate using wire-based laser metal deposition. In order to understand the relationship between the process conditions and the resulting structure properties, detailed analyses of the chemical composition and texture of the structure are performed. Additionally, microhardness mapping was conducted to precisely understand the effects of the developed microstructural features. It is observed that a preferred grain growth orientation proceeding parallel to the building direction using a unidirectional deposition strategy with constant process parameters took place. Indeed, the grain orientation as well as its size and shape are not isotropic within the whole structure. The microstructure contains different grain orientations as well as grain shapes and sizes along the LMD structure. This results in locally different material properties. The results were analysed and discussed in reference to fundamental theories such as the Hall-Petch and Orowan mechanisms. Due to the process conditions, three distinct areas within the structure were observed. It is shown that the LMD area near the substrate is strongly influenced by the microstructure of the used substrate material. With increasing distance to the substrate, the LMD structure shows a directional grain growth in building direction. This directional grain growth changes into globular grain growth with increasing distance to the centre of the part, which represents a change of heat conduction and cooling conditions.

Keywords: laser additive manufacturing; laser metal deposition, aluminium alloy; microstructure; EBSD; mechanical properties.

1. Introduction

In times of globalization and huge demands on environmentally compatible public transportation systems, fuel saving became one of the most pursued optimization fields in automotive, naval architecture and aircraft industry [1]. Therefore, using highly efficient materials for weight reduction is a major demand. Hence, materials with a high strength-to-density ratio were developed and implemented [2]. Due to their recyclability, excellent strength-to-density ratio, thermal and electrical conductivity, corrosion resistance, formability, and attractive appearance, aluminium alloys became one of the most commonly used materials [1, 3, 4].

Simultaneously, additive manufacturing (AM) techniques of powder and wire raw material was strongly investigated

during the last decades [5]. In case of aluminium, predominantly powder-based techniques such as selective laser melting (SLM) were developed and investigated [3, 6, 7, 8]. At this juncture, mostly the near-eutectic Si containing AlSi10Mg and Al12Si alloys, which were developed for casting processes, were processed [9]. Using these alloys in SLM, it was possible to produce highly complex shaped parts at a deposition rate of around 86 g/h [10]. However, the range of aluminium alloys available as qualified powder for SLM is very limited. Laser metal deposition (LMD) using conventional wire instead of powder material increasingly reached the focus of attention [5, 11]. This technique opens a larger range of commercially available alloys, which are already disposable as wire. Additionally, a significantly increasable deposition rate, material usability and easy handling of the consumable material compared to SLM can be realized. Using this method it is possible to produce parts with a deposition rate of more than 1330 g/h, 15 times higher than conventional SLM [12]. Indeed, because of its good weldability and excellent

*Corresponding author

Email address: martin.froend@hzg.de (M. Froend)

mechanical properties, mostly titanium alloys and Inconel were applied and investigated [13, 14, 15, 16]. Until today, only in [12] the proven processability of wire-based LMD to process aluminium alloys was educed.

On the one hand, a higher laser power input of several kilowatts is required for wire-based LMD when compared to powder-based approaches with only a few hundred Watts. This immense increase of specific process energy in connection with the possible high deposition rates, led to new challenges regarding the temperature controllability within the process. On the other hand, using laser energy source instead of arc, as a very good controllable energy input, opens a new field of online process modification possibilities of the final part properties by i.e. varying the heat input or cooling conditions during the process, connected to high throughput part generation. Compared to electron beam only local shielding gas supply can be used instead of conducting the process under vacuum conditions. Especially by taking into account that the process parameters such as the deposition rate and the deposition strategy together with the heat distribution during the process have a significant impact on the residual stresses and final part properties [17, 18, 19, 20], the approach of using wire-based LMD opens a wide field of degrees of freedom in AM.

In conventional manufacturing processes, the final part properties strongly depend on the supplied raw material properties. In AM local material properties can be influenced by using different process parameters, which can also lead to the development locally different mechanical properties of the LMD structure compared to the raw material. Especially the high degree of freedom to process the materials with different process parameters, such as laser power, wire-feeding speed, deposition velocity or strategy in order to develop locally different material properties allows it to build highly complex parts with functionally graded properties in one process [17, 19, 21, 22, 23, 24, 25]. Objective of the present study is the investigation of microstructural and mechanical properties of LMD processed AA5087 on an AA5754 substrate regarding grain size, grain morphology, chemical composition, microtexture and microhardness.

2. Laser metal deposition using filler wire

In this study, the aluminium alloys AlMg4.5MnZr (EN AW-5087) in H19 condition as wire and AlMg3 (EN AW-5754) rolled substrate sheet in annealed and recrystallized (H111) condition were used for LMD experiments. Table 1 shows the chemical composition as well as the mechanical properties of the raw material.

An 8 kW continuous wave ytterbium fibre laser YLS-8000-S2-Y12 (IPG Photonics Corporation) integrated with an optical head YW52 Precitec, which was implemented in a CNC-supported XYZ-machining centre (IXION Corporation PLC), was used in the experiments. Figure 1 visualizes the deposition process of the wall structure, whereas

AA5087 Wire Material(H19)										
Si	Fe	Cu	Mn	Mg	Cr	Zn	Zr	Ti	Al	
≤ 0.40	≤ 0.40	≤ 0.10	≤ 0.50	$2.60 \leq 3.60$	≤ 0.30	≤ 0.20	-	≤ 0.15	Bal.	
ρ	E	R _m	R _{p0.2}	A	HV0.2					
[g/cm ³]	[GPa]	[MPa]	[MPa]	[MPa]	[MPa]	[%]				
2.66	70	440	430	1	135					
AA5754 Substrate Material(H111)										
Si	Fe	Cu	Mn	Mg	Cr	Zn	Zr	Ti	Al	
≤ 0.25	≤ 0.40	≤ 0.05	$0.70 \leq 1.10$	$4.50 \leq 5.20$	$0.05 \leq 0.25$	≤ 0.25	$0.20 \leq 1.10$	≤ 1.15	Bal.	
ρ	E	R _m	R _{p0.2}	A	HV0.2					
[g/cm ³]	[GPa]	[MPa]	[MPa]	[MPa]	[MPa]	[%]				
2.66	70	245	185	15	52					

Table 1: Chemical composition (in wt.%) of AA5087 wire material and AA5754 substrate material, as well as its mechanical properties: Density ρ , Young's modulus E, yield strength R_m, tensile strength R_{0.2}, strain to fracture A and microhardness HV [26, 27].

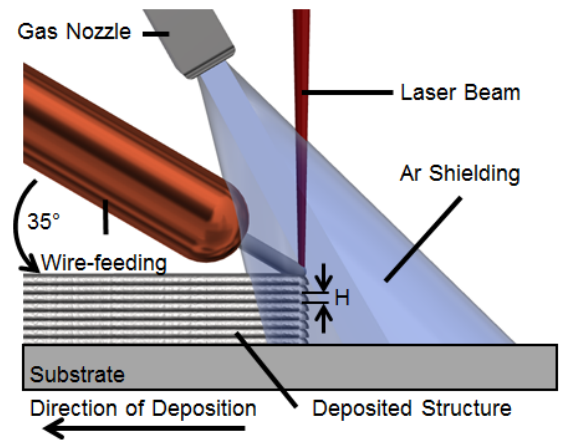


Figure 1: Schematic visualization of the LMD process showing also the unidirectional deposition strategy on top of each layer.

the LMD process parameters used in this study are given in Table 2. The optical head was mounted on the Z-axis of the system, which was also equipped with a wire-feeding system and a local argon shielding gas supply. The wire was fed onto the workpiece using a feeding angle of 35°. The LMD process was conducted by feeding the wire in dragging configuration onto the workpiece while melting it simultaneously by the laser beam. During this, the optical head was moved relatively to the transverse direction of the substrate, which was the deposition direction. After the deposition of one layer, the optical system together with the wire supply was adjusted to the top of the structure again, repeating the deposition process in the same direction as for the previous bead. The following layer was deposited approximately 30 seconds after finishing the previous one. It was shown in [12] that these parameters achieve defect free structures, which could also be confirmed during the experiments within this study.

2.1. Methods for Microstructural Investigations

The microstructure of the processed AA5087/AA5754 structure is investigated by scanning electron microscopy (Jeol JSM-6490LV) using energy dispersive X-ray analysis

Property	Value	Unit
Wavelength	1.070	μm
Beam Parameter Product	11.305	mm mrad
Fibre Diameter	300	μm
Focal Length	300	mm
Collimator Length	150	mm
Laser Spot Diameter (in Focus)	746	μm
Rayleigh Length	24.55	mm
Focus Position	+23	mm
Spot Diameter (in Focus +23 mm)	1.6	mm
Laser Power	4500	Watt
Depositioning Rate	5	m/min
Specific Energy	34	J/g
Wire Feeding Rate	10	m/min
Substrate Temperature	300	$^{\circ}\text{C}$
Argon Shielding Gas Flow Rate	13	l/min
Height Offset per Layer (H)	0.5	mm
Number of Layers	8	–

Table 2: Design parameters of the laser system and applied process parameters in LMD experiments.

EDX (EDAX genesis), to examine chemical composition of heterogeneous microstructure constituents. The EDX analysis has been conducted at 15 kV and working distance of 10 mm during a predetermined measurement time of 150 s. Electron back scatter diffraction (EBSD, EDAX TSL OIM) is applied to analyze microtextures. For EBSD measurements performed at 30 kV, working distance of 13 mm and sample tilt of 70° , a scan field with a size of $950 \mu\text{m}$ by $950 \mu\text{m}$ was defined to achieve a sufficient grain statistic. The orientation calculation was conducted based on the generalized spherical harmonic expansion method [28], where a triclinic sample symmetry was assumed. Figure 2 shows the cross section of the LMD processed wall structure as well as the identification of three locations, which are investigated using EDX and EBSD measurements. For the analyses, the metallographic specimen was prepared by multistage grinding and subsequent final polishing. The measuring locations for EDX and EBSD analyses are indicated as regions A–C. Region A lies in the AA5754 substrate. Region B captures the interface between AA5754 substrate and deposited AA5087 structure, including the heat affected zone (HAZ) in the substrate and the LMD layer close to the substrate. Region C enables the consideration of deposited AA5087 structure at sufficient distance to the substrate, which represents a position at the topside of the structure. RD describes the rolling direction of AA5754 sheet used as substrate and the thickness direction of deposited structure. TD (transverse direction) represents the thickness direction of the substrate and LMD building direction into structure height. ND (normal direction) is perpendicular to the cross section of the grinded and polished specimen. Crystal orientation maps as well as inverse [001] pole figures were mainly used

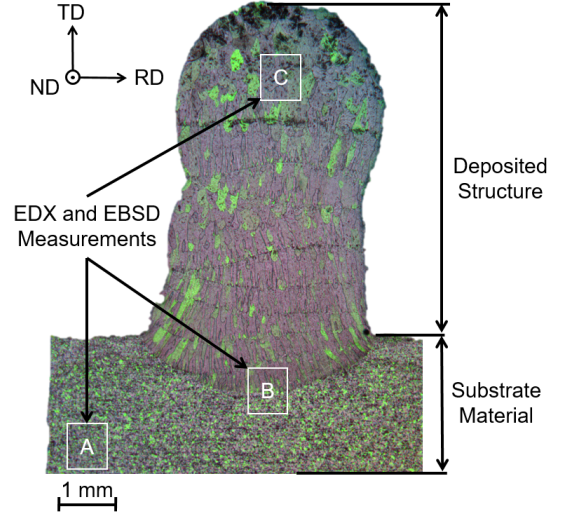


Figure 2: Measurement locations in EDX and EBSD A (substrate material), B (HAZ and first LMD layer) and C (LMD structure near the topside of the structure).

to identify crystal direction $\langle u \ v \ w \rangle // \text{ND}$.

Microhardness measurements were obtained using an automated Vickers hardness testing machine at 0.2 kg load and an indentation time of 10 s. The indentations were conducted with a spacing of $250 \mu\text{m}$ between each other. By using a grid measuring pattern, the complete microhardness distribution along the specimen was determined.

3. Results and Discussion

3.1. Analysis of chemical composition and microstructure of as-received AA5754 substrate

The microstructure of the AA5754 substrate is characterized by aluminium grains, small dispersoids and inclusions elongated parallel to the rolling direction. Figure 3a indicates the observed constituent parts and Table 3 shows their chemical compositions. The EDX analysis indicates that needlelike inclusions exhibited higher contents of Si, Mn and Fe compared with the grain matrix. Within the inclusions, Fe content is significantly higher than in the aluminium grains. These grains mainly contain Mg and soluted Si, Mn and Fe in comparably lower amounts. The chemical composition of dispersoids is similar to that of the inclusions.

The surface of the drawn AA5087 wire, shown in Figure 3b reveals deep score marks and included particles. EDX point analysis of these delivered high contents of Mn and Fe. The wire matrix consists of Al, Mg, Mn, Fe and Zr in agreement to the nominal chemical composition of AA5087 [26].

Within the binary Al-Fe system of the substrate material, aluminium and ferrite form the intermetallic Al_3Fe phase precipitated as randomly distributed acicular crystals in the AA5754 matrix [29][30]. When the detected

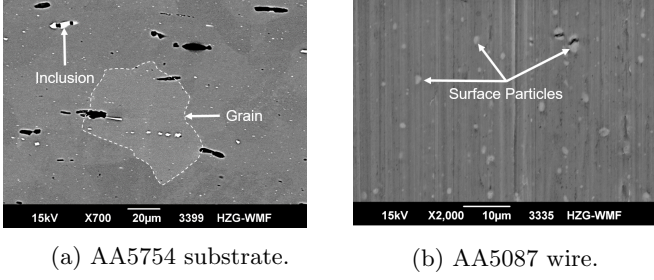


Figure 3: Microstructure of substrate within the region A (a) and surface structure of wire (b) prior to LMD with an identification of the point analyses locations.

Mn will be taken into account because of its content of 3.92 wt.%, the needlelike inclusions can be described as $\text{Al}_3(\text{Fe},\text{Mn})$ phase. Taking this into account, the substrate material is identified as $\text{AlMg}_3\text{SiMnFe} + \text{Al}_3(\text{Fe},\text{Mn})$, which conforms to the composition of AA5754 [27]. The precipitation of the Al_8Mg_5 phase in cold-formed AlMg alloys, having more than 3 to 4 wt.% Mg takes place after a long period of artificial ageing. The Al_8Mg_5 phase is not present in the substrate.

The recrystallized substrate microstructure prior to LMD

AA5087 Wire Material (Figure 3b)							
Elements	Mg	Al	Si	Mn	Fe	Cu	
Surface Particles	2.38	77.35	0.01	13.14	6.57	0.39	
Surface Matrix	5.48	93.19	0.02	0.59	0.22	0.18	
AA5754 Substrate (Figure 3a)							
Elements	Mg	Al	Si	Mn	Fe	Zr	Cu
Inclusions	0.90	63.21	0.65	3.92	31.31	-/-	-/-
Matrix	3.40	95.98	0.07	0.37	0.18	-/-	-/-
Dispersoids	3.11	89.96	0.26	2.19	4.48	-/-	-/-

Table 3: Chemical composition (in wt%) of different phases in substrate and wire material.

is characterized by grains with an average grain length $d_{maj} = 24.10 \mu\text{m}$ and an average grain width $d_{min} = 11.79 \mu\text{m}$, i.e. the grains reveal an elliptical shape as can be seen in Fig. 4a with an resulting average aspect ratio d_{asp} of $d_{min}/d_{maj} \approx 0.50$. The grain shape orientation describes the angular relationship between major axis d_{maj} of the ellipsoidal shaped grains and the horizontal direction RD. The statistical assessment of this relationship shows that a morphologically preferred alignment of the grains does not exist as seen by the appearance of various maxima, Figure 4b. A possible explanation for this is that the recrystallization process changed the grain shape of the cold-rolled sheet during annealing in order to minimize grain boundary energy [31].

The inverse $[001]$ pole figure of the substrate shows that the majority of grains are oriented in $\langle 101 \rangle // [001]$ direction. Furthermore, grain orientations of $\langle 111 \rangle // [001]$, $\langle 112 \rangle // [001]$ and $\langle 001 \rangle // [001]$ were detected. $\langle 101 \rangle$ and $\langle 001 \rangle$ are connected with each other with an orientation band. This is plotted in Figure 5 showing an

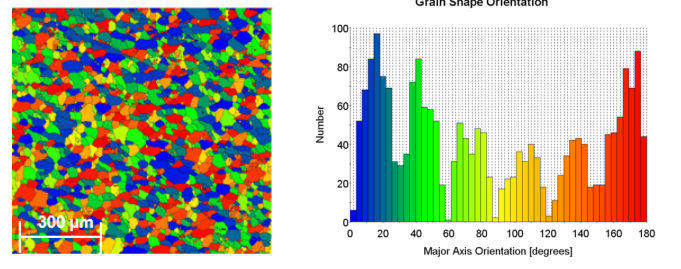


Figure 4: Grain map of AA5087 substrate (a) and the distribution with respect to the major axis orientation (d_{maj}).

intensity maximum $H_{max} = 2.369$ mrd. Table 4 summarizes the results regarding crystal directions, microtexture components and grain sizes of AA5754 substrate.

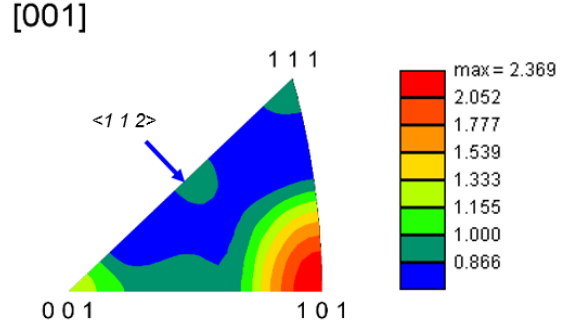


Figure 5: Inverse $[001]$ pole figure of AA5754 substrate intensity maximum $H_{max} = 2.396$ mrd).

AA5754 Substrate	
$\langle u v w \rangle // [001]$	$(h k l)[u v w]$
$\langle 101 \rangle$, $H = 2.36$ mrd	$(110)[001]$, $(110)[1-11]$
$\langle 001 \rangle$, $H = 1.23$ mrd	$(001)[100]$
$\langle 111 \rangle$, $H = 1.00$ mrd	$(111)[-1-12]$
$\langle 112 \rangle$, $H = 1.00$ mrd	$(112)[-1-11]$
$H_{max} = 2.396$ mrd	
Grain size	
$d_{maj} = (24.10 \pm 8.89) \mu\text{m}$	
$d_{min} = (11.79 \pm 4.32) \mu\text{m}$	
$d_{asp} = (0.50 \pm 0.11) \mu\text{m}$	

Table 4: Results of EBSD analyses of the AA5754 substrate before LMD (region A).

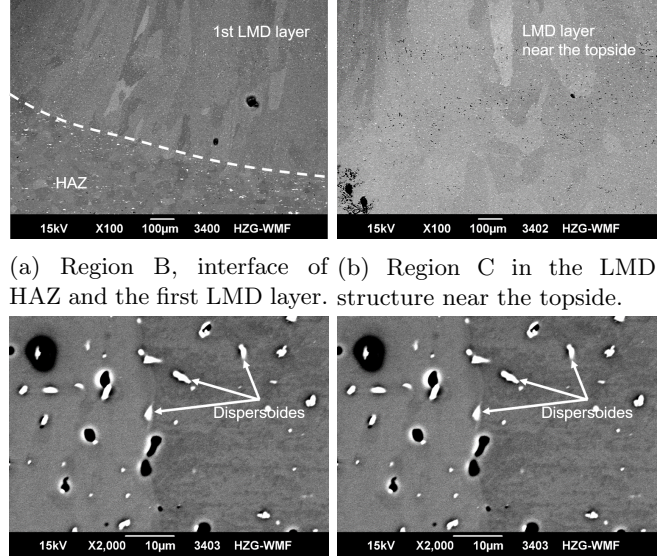
3.2. Microstructural characterization of laser metal deposited AA5087/AA5754

The microstructure of the LMD structure shows a statistically even distribution of small particles, Figures 6a–6d. Their dimensions d of $\leq 5 \mu m$ are significantly lower compared with the inclusions both in the HAZ or substrate. The LMD structure exhibits higher contents of Mg and Mn than the HAZ as expected and corresponds to AA5087 used as wire [26]. The particles included within the LMD layer reveal higher contents of Fe, Mn and Si compared with matrix material. Their origin is assumed to come from the wire, on which particles with a matching chemical composition at the wire surface were found (Figure 6c, Table 3). It is assumed that Si migrated from inclusions and dispersoids of the substrate to the first LMD layers close to the substrate. The Si contents decreases with increasing number of layers (Table 5). The alloying element Cu as integral part of the wire was also detected. However, it showed contents below the limit detectable by the EDX system. Therefore, Table 5 does not show any value regarding Cu.

According to [32] an increase of Mg content from 3 wt.% to 4.5 wt.% results in an increase of tensile strength from 208 MPa to 250 MPa and an increase of the yield strength from 96 MPa to 117 MPa [32]. Manganese has also a strength increasing effect. The transition from the HAZ of the substrate to the deposited AA5087 LMD layer is characterized by a strongly pronounced discontinuity (Figures 6a and 7a). The elliptically shaped grains of the HAZ exhibit an average grain length of $d_{maj} = 23.01 \mu m$ and an average grain width of $d_{min} = 11.24 \mu m$ as well as an aspect ratio d_{min}/d_{maj} of 0.50. This means, the morphological grain alignment in the HAZ is comparable with the as-received condition of the substrate (Table 4), i.e. the heat input during LMD process did not change significantly the grain size and morphology, respectively (Table 6).

However, it was observed that the LMD process led to strong distortion of the substrate. Thus, the axial intensity of the crystal direction $\langle 1 0 1 \rangle // [0 0 1]$ became lower and an additional orientation direction through $\langle 3 1 3 \rangle // [0 0 1]$ developed in conjunction with a connection line between $\langle 1 0 1 \rangle$ and $\langle 1 1 1 \rangle$ (Figure 7c). The crystal direction $\langle 1 0 1 \rangle // [0 0 1]$ in the HAZ can be assigned to the microtexture component $(1 1 0)[-19 -16 16]$. The calculation of misorientation between the components $(1 1 0)[0 0 1]$ and $(1 1 0)[1 -1 1]$ of the base material as well as $(3 3 -1)[2 5 21]$ of the HAZ leads to angles of 14.5° and 50.2° , respectively. The misorientation between $(1 1 0)[1 -1 1]$ and $(1 1 0)[-19 -16 16]$ is determined as 5.2° , which implies a slight crystal rotation around the normal direction ND.

These misorientations imply that a HAZ in AA5087 substrate is actually present, although Al alloys do not show allotropic phase transformation. Insofar, the local change in microstructure is considered as result of plastic deformation due to thermally induced distortion during the LMD process. This effect is also known as temperature gradient mechanism and a well known challenge in laser process-



(a) Region B, interface of HAZ and the first LMD layer. (b) Region C in the LMD structure near the top side. (c) Region B, interface HAZ to the 1st LMD layer. (d) Region C in the LMD structure near the top side.

Figure 6: Measuring location B, which shows the transition zone between HAZ and the first LMD layer with a magnification of 100 (a) and a magnification of 2000 showing also the identification of the measured points in EDX (b), as well as a LMD layer near the top side of the structure (Region C) with a magnification of 100 (c) and a magnification of 2000 (d).

ing of metallic materials such as laser beam welding [33]. Therefore, the distortion of the substrate, which changed the grain orientation near the first LMD layer results in a HAZ.

The microstructure of deposited AA5087 layer adjacent to the HAZ consist of dendritic grains and is coarser compared with the microstructure of the HAZ or the base material of the substrate. The average grain length $d_{maj} = 110.36 \mu m$, average grain width $d_{min} = 23.19 \mu m$ and an resulting aspect ratio $d_{min}/d_{maj} = 0.26$ were determined, Figure 7a. The major axis of dendritic grains is almost parallel to the building direction of the structure. They are aligned between 70° and 120° with respect to TD, which can also be seen from Figure 7b. Within the dendritically solidified LMD layer, the main crystal directions $\langle 1 0 1 \rangle // [0 0 1]$, $\langle 3 0 4 \rangle // [0 0 1]$, $\langle 1 1 5 \rangle // [0 0 1]$, $\langle 0 1 5 \rangle // [0 0 1]$, $\langle 0 0 1 \rangle // [0 0 1]$ were detected (Figure 7d). The calculation of misorientation between the components $(1 1 0)[0 0 1]$ and $(1 1 0)[1 -1 1]$ of the base material as well as $(0 4 3)[1 -3 4]$ of the dendritic LMD layer yields in angles of 45.9° and 56.2° , respectively.

The dendritic microstructure of LMD layer shows a further grain coarsening with increasing LMD structure height to an average grain length $d_{maj} = 141.93 \mu m$, an average grain width $d_{min} = 50.56$ and an resulting aspect ratio $d_{min}/d_{maj} = 0.28$ (Figure 7e). This observations also show a horizontal grain coarsening with increasing distance to the centre of the structure. Similar to the LMD layer adjacent to the HAZ the long axis of dendritic

Elements	Mg	Al	Si	Mn	Fe	Zr
	3.76	95.09	0.32	0.22	0.34	0.27
Dispersoids within the first LMD Layer (Figure 6c)						
	4.33	81.22	1.67	2.36	10.21	0.22
Matrix of the first LMD Layer (Figure 6c)						
	4.12	94.58	0.08	0.59	0.39	0.23
Dispersoids within the Topside (Figure 6d)						
	2.85	76.29	0.53	7.39	12.78	0.16
Matrix of the Topside (Figure 6d)						
	4.57	94.08	0.06	0.85	0.19	0.26

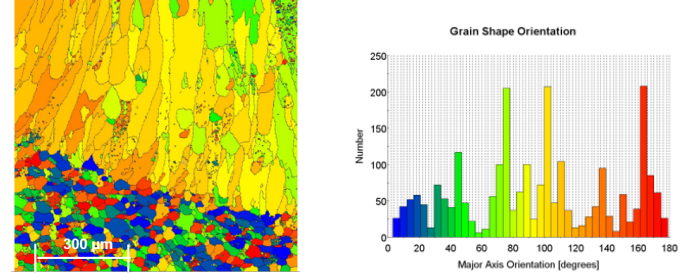
Table 5: Chemical composition (wt.%) of HAZ in (Figure 6a) and LMD layer regarding matrix and particles (Figures 6b – 6d).

grains is mainly aligned between 60° and 100° , Figure 7f. The inverse $[0\ 0\ 1]$ pole figure shows a high axial intensity at $\langle 1\ 0\ 3 \rangle // [0\ 0\ 1]$ and $\langle 1\ 1\ 1 \rangle // [0\ 0\ 1]$, Figure 7g. This indicates a considerable deviation from the microstructure of the LMD layer adjacent to the HAZ. The results obtained by EBSD analysis are summarized in Table 6.

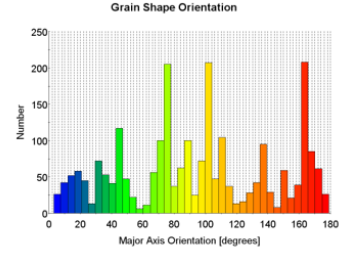
$\langle u\ v\ w \rangle // [0\ 0\ 1]$	$(h\ k\ l)[u\ v\ w]$	Grain size
Heat affected zone (HAZ)		
$\langle 1\ 0\ 1 \rangle$, $H = 1.76$ mrd	$(1\ 1\ 0)[-19\ -16\ 16]$	$d_{maj} = (23.01 \pm 8.41)\ \mu\text{m}$
$\langle 3\ 1\ 3 \rangle$, $H = 1.95$ mrd	$(3\ 3\ -1)[2\ 5\ 21]$	$d_{min} = (11.24 \pm 4.14)\ \mu\text{m}$
$\langle 1\ 1\ 1 \rangle$, $H = 1.13$ mrd	$(1\ 1\ 1)[23\ -14\ 9]$	$d_{asp} = (0.50 \pm 0.11)\ \mu\text{m}$
$H_{max} = 2.018$ mrd		$f_{max} = 6.988$ mrd
Interface of HAZ to first Layer		
$\langle 1\ 0\ 1 \rangle$, $H = 2.10$ mrd	$(0\ 1\ 1)[1\ 0\ 0]$	$d_{maj} = (110.36 \pm 38.73)\ \mu\text{m}$
$\langle 3\ 0\ 4 \rangle$, $H = 2.09$ mrd	$(0\ 4\ 3)[1\ -3\ 4]$	$d_{min} = (23.19 \pm 7.90)\ \mu\text{m}$
$\langle 1\ 1\ 5 \rangle$, $H = 1.68$ mrd	$(1\ 1\ 5)[2\ -7\ 1]$	$d_{asp} = (0.26 \pm 0.14)\ \mu\text{m}$
$\langle 0\ 1\ 5 \rangle$, $H = 1.50$ mrd	$(0\ 1\ 5)[11\ -25\ 5]$	$f_{max} = 16.075$ mrd
$\langle 0\ 0\ 1 \rangle$, $H = 1.12$ mrd	$(0\ 0\ 1)[1\ 0\ 0]$	
$H_{max} = 2.121$ mrd		
Topside of the structure		
$\langle 1\ 0\ 1 \rangle$, $H = 1.99$ mrd	$(0\ 1\ 1)[-1\ -3\ 3]$	$d_{maj} = (141.93 \pm 48.30)\ \mu\text{m}$
$\langle 1\ 1\ 1 \rangle$, $H = 1.74$ mrd	$(1\ 1\ 1)[5\ -7\ 2]$	$d_{min} = (50.56 \pm 17.69)\ \mu\text{m}$
$\langle 0\ 0\ 1 \rangle$, $H = 1.39$ mrd	$(0\ 0\ 1)[5\ -7\ 0]$	$d_{asp} = (0.38 \pm 0.13)\ \mu\text{m}$
$\langle 1\ 0\ 3 \rangle$, $H = 2.24$ mrd	$(0\ 3\ 1)[1\ 0\ 0]$	$f_{max} = 15.932$ mrd
$H_{max} = 2.277$ mrd		

Table 6: Crystal orientations and grain morphology both in HAZ and LMD structure.

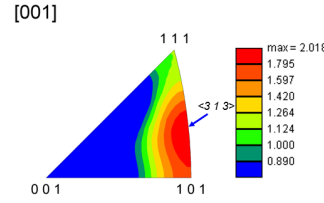
The average grain size in the topside of the structure increased and the entire LMD microstructure is significantly coarser compared with the microstructure of the substrate or HAZ, respectively. The average dendrites width of $23.19\ \mu\text{m}$ in the first LMD layer adjacent to the HAZ and the average grain length of $23.01\ \mu\text{m}$ of the substrate are almost identical. Hence, heteroepitaxial growth of the AA5087 layer has taken place on the AA5754 substrate during the first stages of LMD process. The correlation between the substrate and the deposited LMD layer near the HAZ in building direction, which is parallel to TD can



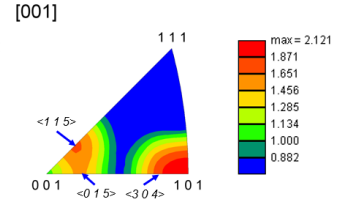
(a) Grain shape orientation map of HAZ to the first LMD layer interface (region B).



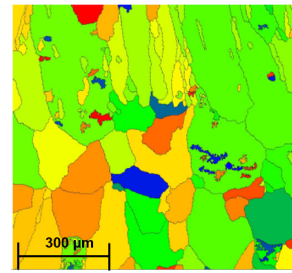
(b) Grain shape distribution plot of HAZ to the first LMD layer interface (region B).



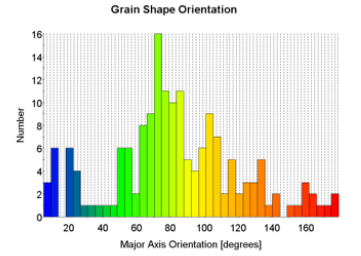
(c) HAZ inverse $[0\ 0\ 1]$ pole figure.



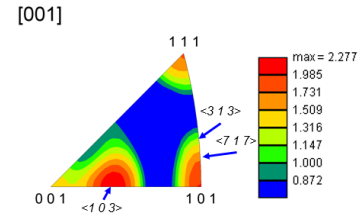
(d) Interface inverse $[0\ 0\ 1]$ pole figure.



(e) Grain shape orientation map at the top of the structure (region C).



(f) Grain shape distribution plot of the top of the structure (region C).



(g) LMD 2 inverse $[0\ 0\ 1]$ pole figure.

Figure 7: Grain map of the interface between HAZ and the first LMD layer (a), the orientation distribution regarding the major axis orientation (d_{maj})(b), the inverse $[0\ 0\ 1]$ pole figure of the HAZ ($H_{max} = 2.018$ mrd) (c), the inverse $[0\ 0\ 1]$ pole figure of the first LMD layer near the HAZ ($H_{max} = 2.121$ mrd)(d), microstructure at the top of the structure (e), the orientation distribution regarding the major axis orientation (d_{maj}) (f) and the inverse $[0\ 0\ 1]$ pole figure in the top of the structure ($H_{max} = 2.277$ mrd) (g).

315 be approximately described by $\langle 1\ 0\ 0 \rangle_{BM} // \langle 1\ 0\ 0 \rangle_{Layer}$
 (Figures 8a and 8b). The building direction parallel to TD
 can be considered as main growth direction of the dendritic³⁵⁰
 grains during solidification because long axis of dendritic
 grains (d_{maj}) and building direction TD are almost paral-
 320 lel to one another. In [34], it was reported that a preferred
 crystallographic orientation is formed, when unidirectional
 solidification occurs during chill casting. The growth of
 aluminium crystals is fast in $\langle 1\ 0\ 0 \rangle$ direction and the re-
 sult of unidirectional solidification shows a $\langle 1\ 0\ 0 \rangle$ fiber
 325 texture. Figure 8b shows $\langle 1\ 0\ 0 \rangle$ pole figures, which con-
 tain an indication of the presence of a local $\langle 1\ 0\ 0 \rangle$ fibre
 texture. Therefore, it can be assumed that the deposition
 of AA5087 wire met the conditions of solidification after
 direct chill casting locally during the first sequences of the
 330 LMD process.

The local $\langle 1\ 0\ 0 \rangle$ fibre texture implies that the heat trans-
 fer was mainly determined by the $\langle 1\ 0\ 0 \rangle$ crystal growth in
 opposite direction. It must be stated that the orientation
 belt on the RD axis of the $\langle 1\ 0\ 0 \rangle$ pole figure is not tightly
 335 closed, because the use of EBSD method recorded only a
 small region of LMD layer microstructure near the HAZ
 limiting the number of possible orientations.

The further grain coarsening can be explained due to de-
 creasing cooling rate with increasing LMD structure height.
 340 In the LMD layers near the substrate the heat is conducted
 into the substrate, whereas a heat accumulation with in-
 creasing distance to the substrate took place. The increas-
 ing distance to the substrate as well as the already heated
 underlying layer sequences lead to a slowdown of cooling
 345 and decrease of critical undercooling important for hetero-
 geneous nucleation. The microstructure near the topline
 (Figure 7e) formed a strongly randomized microtexture.
 The $\langle 0\ 0\ 1 \rangle$ pole figure does not show any preferred orienta-
 tion and indicates an isotropic distribution of heat transfer
 (Figure 8c).

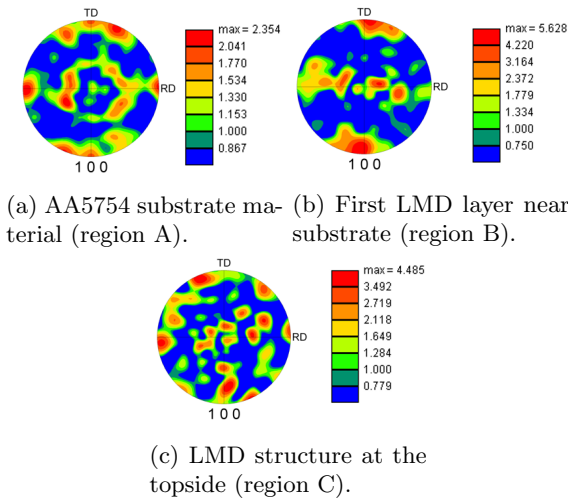


Figure 8: $\langle 1\ 0\ 0 \rangle$ pole figures at the measuring location A – C of the specimen including the AA5754 substrate (a), the deposited AA5087 layer near the HAZ (b) and the deposited AA5087 layer near the topline of the structure (c).

3.3. Microhardness and mechanical properties

Since there is a linear relationship between the micro-
 hardness and tensile strength of a material, the microhard-
 ness of the LMD-structure was analysed and used to de-
 rive inferences to its tensile properties. The microhardness
 of the wire material was 135 HV, whereas the substrate
 material showed a microhardness of 52 HV in as-received
 condition, see Table 1. Figs. 9 and 10 show the hardness
 distribution of the LMD processed structure. Regarding
 the HAZ and the area, where the wire diluted into the
 substrate, a significant increase up to 69 HV is observed.
 Along the HAZ into the first LMD layers, the hardness also
 increased significantly. As also can be seen from Figure 10,
 the hardness slightly decreases after the third layer from 72
 HV to 67 HV within the 4th to the 8th layer. The micro-
 hardness distribution in RD direction respectively along
 the width of the specimen showed no significant changes.

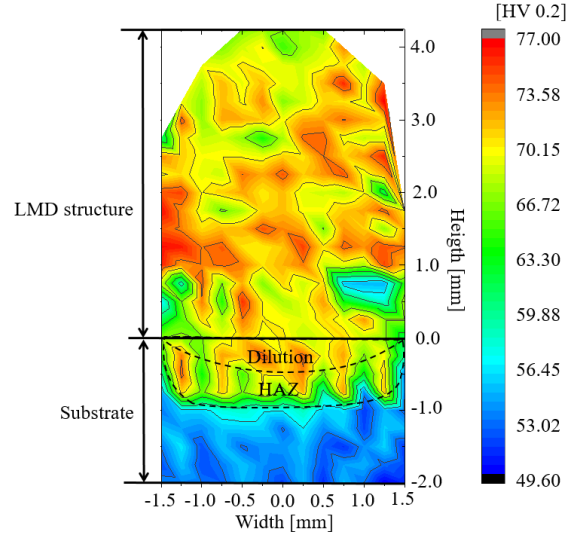


Figure 9: Results of microhardness mapping.

From EBSD, EDX and microhardness testing, three dif-
 ferent contributions influencing the local strength of the
 deposited structure were detected. Regarding the yield
 strength, these contributions can be summarized as fol-
 lowed:

$$\Delta Rp_{0.2} = \underbrace{(k_{i1} \sqrt{n_{FA}})}_A + \underbrace{(3NGbf^{\frac{3}{2}}r^{-1})}_B + \underbrace{(k_{i2} + k_{i3}D^{-\frac{3}{2}})}_C \quad (1)$$

with

k_{i1} = obstacles strength and the Youngs modulus, n_{FA} =
 ratio of foreign atoms, N = hardness of the surrounding
 matrix, G = shear modulus, b = burger vector, f = the
 volume of the dispersoides, k_{i2} = critical shear stress of
 the mono-crystal, k_{i3} = material dependent Hall-Petch
 constant and D = grain diameter.

Due to an increase of Mg-content from the substrate to the

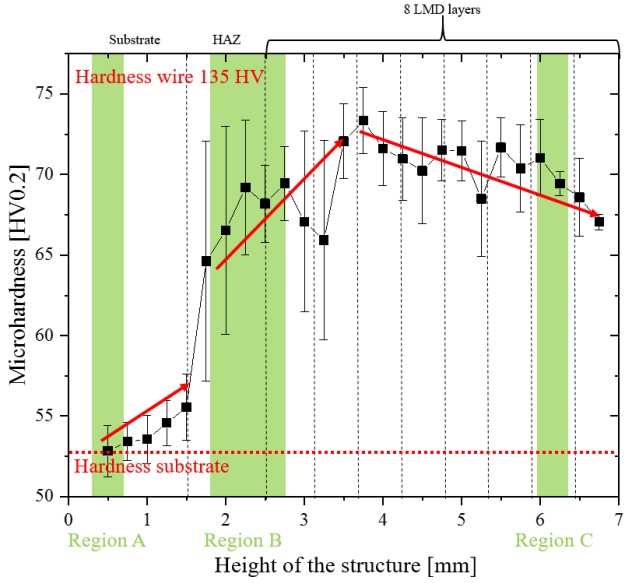


Figure 10: Results of microhardness mapping along the substrate and the deposited wall structure.

LMD-structure a solid solution hardening results. This effect is shown by the first part (A) of equation 1, which mirrors the contribution of foreign atoms to the strength of a material. Thereby, a higher amount of Mg atoms are beneficial in terms of an strengthening effect, which could be confirmed by the detections in EDX analysis. The chemical composition can also be seen from Figure 11. From there it is shown that the Si, Zr, Mn and Fe contents along the structure are constant. Only the Mg content increases from 3.54 to 5.09 wt.% from the substrate to the topside of the LMD structure. Part (B) of equation 1 shows the contribution of the Orowan mechanism, which describes the hardness increase of a material for a high volume of dispersoids within the matrix, similar to precipitation hardening. This is given by the high amount of detected dispersoids within the structure and contributes the solid solution hardening. As EBSD analyses pointed out, the grain morphology along the specimen varies. Regarding the centre of the structure, longitudinal shaped grains developed, whereas the grain morphology in the topside shaped more randomly oriented globular grains. Since the Hall-Petch relation holds, describing the influence of the grain size on the resulting strength this grain coarsening has also an influence of the material properties [35]. In the case of the upper part of the LMD structure, this effect results in a decrease of the microhardness and local strength, which is given by part (C) of equation 1. This effect counteracts to the hardening contributions of parts (A) and (B) in such a way as to weaken the detected hardening effects for the upper part of the LMD-structure. Due to the results of the texture analyses, the local strength in RD direction, which corresponds to the thickness direction of the deposited structure is assumed to be lower than in TD direction. Especially the local strength in the topside of the

structure is assumed to be slightly less, which is reasoned with the grain coarsening with increasing distance to the substrate as shown by the comparison of the aspect ratio of the grains in region B and C of the LMD structure.

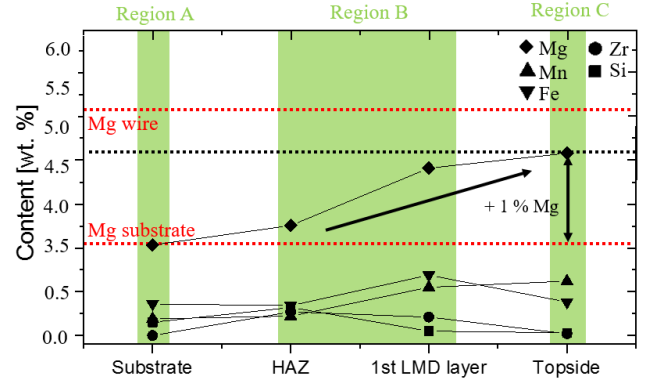


Figure 11: Chemical composition along the height of the structure.

4. Conclusions

It was found that the LMD process led to the formation of an anisotropic AA5087 layer structure regarding grain size, morphology and crystallographic orientation using constant process parameters. Especially the detected grain morphology as well as their orientation has a significant influence on the mechanical properties along the structure. Due to this, three different regions with different properties were identified. The region near the substrate, in the centre of the structure and at the topside of the structure are assumed to exhibit different mechanical properties.

This leads to the conclusion that it is not possible to manufacture a homogeneous structure using constant process parameters in wire-based LMD of AA5087 aluminium. Therefore, further online process adoptions regarding i.e. the energy control, cooling condition or layer height adjustment have to be considered in future investigations. Indeed, the findings show, that wire-based LMD of aluminium enables high deposition rates but also opens new challenges regarding the process temperature controllability, which was exemplified by analysing the heat accumulation in the centre of the structure.

Acknowledgements

This project has received funding from the European Unions Horizon 2020 research and innovation programme under grant agreement No 723600. Additionally, the authors would like to thank Mr. R. Dinse, Mr. P. Haack and Mr. F. Dorn from Helmholtz-Zentrum Geesthacht for their valuable technical support.

References

- [1] Dursun T, Soutis C. Recent developments in advanced aircraft aluminium alloys. *Materials and Design* (1980-500 2015) 2014;56:862–71. URL: <http://www.sciencedirect.com/science/article/pii/S0261306913011357>. doi:<http://dx.doi.org/10.1016/j.matdes.2013.12.002>.
- [2] Huang CQ, Deng J, Wang SX, lei Liu L. A physical-based constitutive model to describe the strain-hardening⁵⁰⁵ and dynamic recovery behaviors of 5754 aluminum alloy. *Materials Science and Engineering: A* 2017;699:106–13. URL: <http://www.sciencedirect.com/science/article/pii/S0921509317305567>. doi:<http://dx.doi.org/10.1016/j.msea.2017.04.086>.⁵¹⁰
- [3] Olakanmi E, Cochrane R, Dalgarno K. A review on selective laser sintering/melting (SLS/SLM) of aluminium alloy powders: Processing, microstructure, and properties. *Progress in Materials Science* 2015;74:401–77. URL: <http://www.sciencedirect.com/science/article/pii/S0079642515000389>. doi:<http://dx.doi.org/10.1016/j.pmatsci.2015.03.002>.
- [4] Hong KM, Shin YC. Prospects of laser welding technology in the automotive industry: A review. *Journal of Materials Processing Technology* 2017;245:46–69. URL: <http://www.sciencedirect.com/science/article/pii/S0924013617300523>. doi:<http://dx.doi.org/10.1016/j.jmatprotec.2017.02.008>.⁵²⁰
- [5] Schmidt M, Merklein M, Bourell D, Dimitrov D, Hausotte T, Wegener K, et al. Laser based additive manufacturing in industry and academia. *CIRP Annals - Manufacturing Tech*⁵²⁵ *nology* 2017;URL: <http://www.sciencedirect.com/science/article/pii/S0007850617301506>. doi:<http://dx.doi.org/10.1016/j.cirp.2017.05.011>.
- [6] Kang N, Coddet P, Liao H, Baur T, Coddet C. Wear behavior and microstructure of hypereutectic Al-Si alloys prepared by⁵³⁰ selective laser melting. *Applied Surface Science* 2016;378(Supplement C):142–9. URL: <http://www.sciencedirect.com/science/article/pii/S0169433216307140>. doi:<https://doi.org/10.1016/j.apsusc.2016.03.221>.
- [7] Kimura T, Nakamoto T. Microstructures and mechanical⁵³⁵ properties of A356 (AlSi7Mg0.3) aluminum alloy fabricated by selective laser melting. *Materials and Design* 2016;89(Supplement C):1294–301. URL: <http://www.sciencedirect.com/science/article/pii/S0264127515306456>. doi:<https://doi.org/10.1016/j.matdes.2015.10.065>.⁵⁴⁰
- [8] Brandl E, Heckenberger U, Holzinger V, Buchbinder D. Additive manufactured AlSi10Mg samples using Selective Laser Melting (SLM): Microstructure, high cycle fatigue, and fracture behavior. *Materials and Design* 2012;34(Supplement C):159–69. URL: <http://www.sciencedirect.com/science/article/pii/S0261306911005590>. doi:<https://doi.org/10.1016/j.matdes.2011.07.067>.
- [9] Spierings AB, Dawson K, Voegtlin M, Palm F, Uggowitzer PJ. Microstructure and mechanical properties of as-processed scandium-modified aluminium using selective laser melting.⁵⁵⁰ *CIRP Annals - Manufacturing Technology* 2016;65(1):213–6. URL: <http://www.sciencedirect.com/science/article/pii/S0007850616300579>. doi:<http://dx.doi.org/10.1016/j.cirp.2016.04.057>.
- [10] Riveiro A, Mejias A, Lusquios F, del Val J, Comesaa⁵⁵⁵ R, Pardo J, et al. Laser cladding of aluminium on AISI 304 stainless steel with high-power diode lasers. *Surface and Coatings Technology* 2014;253(Supplement C):214–20. URL: <http://www.sciencedirect.com/science/article/pii/S0257897214004459>. doi:<https://doi.org/10.1016/j.surfcoat.2014.05.039>.
- [11] Pinkerton AJ. [INVITED] Lasers in additive manufacturing. *Optics and Laser Technology* 2016;78:25–32. URL: <http://www.sciencedirect.com/science/article/pii/S0030399215002765>. doi:<http://dx.doi.org/10.1016/j.optlastec.2015.09.025>; the year of light: optical fiber sensors and laser material processing.
- [12] Froend M, Riekehr S, Kashaev N, Klusemann B, Enz J. Process development for wire-based laser metal deposition of 5087 aluminium alloy using fiber laser. Submitted to *Journal of Manufacturing processes* 2017;.
- [13] Chen Y, Lu F, Zhang K, Nie P, Hosseini SRE, Feng K, et al. Investigation of dendritic growth and liquation cracking in laser melting deposited Inconel 718 at different laser input angles. *Materials and Design* 2016;105:133–41.
- [14] Zhong M, Liu W. Laser surface cladding: the state of the art and challenges. *Proceedings of the Institution of Mechanical Engineers, Part C: Journal of Mechanical Engineering Science* 2010;224(5):1041–60.
- [15] Szost BA, Terzi S, Martina F, Boisselier D, Prytuliak A, Pirling T, et al. A comparative study of additive manufacturing techniques: Residual stress and microstructural analysis of CLAD and WAAM printed Ti6Al4V components. *Materials and Design* 2016;89:559–67. URL: <http://www.sciencedirect.com/science/article/pii/S0264127515305268>. doi:<http://dx.doi.org/10.1016/j.matdes.2015.09.115>.
- [16] Shi X, Ma S, Liu C, Wu Q, Lu J, Liu Y, et al. Selective laser melting-wire arc additive manufacturing hybrid fabrication of Ti-6Al-4V alloy: Microstructure and mechanical properties. *Materials Science and Engineering: A* 2017;684:196–204. URL: <http://www.sciencedirect.com/science/article/pii/S0921509316315659>. doi:<http://dx.doi.org/10.1016/j.msea.2016.12.065>.
- [17] Cheng B, Shrestha S, Chou K. Stress and deformation evaluations of scanning strategy effect in selective laser melting. *Additive Manufacturing* 2016;12:240–51. URL: <http://www.sciencedirect.com/science/article/pii/S2214860416300914>. doi:<http://dx.doi.org/10.1016/j.addma.2016.05.007>; special Issue on Modeling and Simulation for Additive Manufacturing.
- [18] Thijs L, Verhaeghe F, Craeghs T, Humbeeck JV, Kruth JP. A study of the microstructural evolution during selective laser melting of Ti6Al4V. *Acta Materialia* 2010;58(9):3303–12. URL: <http://www.sciencedirect.com/science/article/pii/S135964541000090X>. doi:<http://dx.doi.org/10.1016/j.actamat.2010.02.004>.
- [19] Read N, Wang W, Essa K, Attallah MM. Selective laser melting of AlSi10Mg alloy: Process optimisation and mechanical properties development. *Materials and Design* (1980-2015) 2015;65:417–24. URL: <http://www.sciencedirect.com/science/article/pii/S0261306914007468>. doi:<http://dx.doi.org/10.1016/j.matdes.2014.09.044>.
- [20] Gupta A, Lloyd D, Court S. Precipitation hardening in AlMgSi alloys with and without excess Si. *Materials Science and Engineering: A* 2001;316(1):11–7. URL: <http://www.sciencedirect.com/science/article/pii/S0921509301012473>. doi:[http://dx.doi.org/10.1016/S0921-5093\(01\)01247-3](http://dx.doi.org/10.1016/S0921-5093(01)01247-3).
- [21] Lima D, Mantri S, Mikler C, Contieri R, Yannetta C, Campo K, et al. Laser additive processing of a functionally graded internal fracture fixation plate. *Materials and Design* 2017;130:8–15. URL: <http://www.sciencedirect.com/science/article/pii/S0264127517305154>. doi:<http://dx.doi.org/10.1016/j.matdes.2017.05.034>.
- [22] Levy A, Miriyev A, Elliott A, Babu SS, Frage N. Additive manufacturing of complex-shaped graded TiC/steel composites. *Materials and Design* 2017;118:198–203. URL: <http://www.sciencedirect.com/science/article/pii/S026412751730031X>. doi:<http://dx.doi.org/10.1016/j.matdes.2017.01.024>.
- [23] Catchpole-Smith S, Aboulkhair N, Parry L, Tuck C, Ashcroft I, Clare A. Fractal scan strategies for selective laser melting of unweldable nickel superalloys. *Additive Manufacturing* 2017;15:113–22. URL: <http://www.sciencedirect.com/science/article/pii/S221486041630358X>. doi:<http://dx.doi.org/10.1016/j.addma.2017.02.002>.
- [24] Lu Y, Wu S, Gan Y, Huang T, Yang C, Junjie L, et al. Study on the microstructure, mechanical property and residual

- stress of SLM Inconel-718 alloy manufactured by differing island scanning strategy. *Optics and Laser Technology* 2015;75:197 – 206. URL: <http://www.sciencedirect.com/science/article/pii/S0030399215002108>. doi:<http://dx.doi.org/10.1016/j.optlastec.2015.07.009>.
- [25] Thijs L, Kempen K, Kruth JP, Humbeeck JV. Fine-structured aluminium products with controllable texture by selective laser melting of pre-alloyed AlSi10Mg powder. *Acta Materialia* 2013;61(5):1809 –19. URL: <http://www.sciencedirect.com/science/article/pii/S1359645412008592>. doi:<http://dx.doi.org/10.1016/j.actamat.2012.11.052>.
- [26] Elisental D. Technical data of AA 5087, supplier information sheet. Elisental 2017;URL: http://www.elisental.de/pdf_de/Aluminium-Draht_Werkstofftabelle_Einlage.pdf.
- [27] Matweb.com . Technical data of AA 5754, information sheet. Matweb 2017;URL: <http://www.matweb.com/search/DataSheet.aspx?MatGUID=bb191b05a9424da5bdef4be5cad33182&ckck=1>.
- [28] H.J.Bunge C. Reproducible Textures. *Textures and Microstructures* 1982;5:87–94.
- [29] Kumar S, Babu NH, Scamans GM, Eskin DG, Fan Z. Solidification behaviour of an AA5754 Al alloy ingot cast with high impurity content. *International Journal of Materials Research* 2012;103(10):1228–34.
- [30] Kramer C. *Aluminium Taschenbuch: Grundlagen und Werkstoffe*. 1st ed.; Aluminium-Zentrale Dsseldorf; 1995.
- [31] Engler O. Simulation of Recrystallization and Recrystallization Textures in Aluminium Alloys. In: *Materials Science Forum*; vol. 715. Trans Tech Publ; 2012, p. 399–406.
- [32] Kendig K, Miracle D. Strengthening mechanisms of an Al-Mg-Sc-Zr alloy. *Acta Materialia* 2002;50(16):4165 –75. URL: <http://www.sciencedirect.com/science/article/pii/S1359645402002586>. doi:[http://dx.doi.org/10.1016/S1359-6454\(02\)00258-6](http://dx.doi.org/10.1016/S1359-6454(02)00258-6).
- [33] Froend M, Fomin F, Riekehr S, Alvarez P, Zubiri F, Bauer S, et al. Fiber laser welding of dissimilar titanium (Ti-6Al-4V/cp-Ti) T-joints and their laser forming process for aircraft application. *Optics and Laser Technology* 2017;96(Supplement C):123 –31. URL: <http://www.sciencedirect.com/science/article/pii/S0030399217301688>. doi:<https://doi.org/10.1016/j.optlastec.2017.05.017>.
- [34] Hirsch J. Textures in industrial processes and products. In: *Materials Science Forum*; vol. 702. Trans Tech Publ; 2012, p. 18–25.
- [35] Hansen N. HallPetch relation and boundary strengthening. *Scripta Materialia* 2004;51(8):801 –6. URL: <http://www.sciencedirect.com/science/article/pii/S1359646204003434>. doi:<http://dx.doi.org/10.1016/j.scriptamat.2004.06.002>; viewpoint set no. 35. Metals and alloys with a structural scale from the micrometer to the atomic dimensions.